# Detailed Interference Analysis in Dense mmWave Systems Employing Dual-Polarized Antennas

Dmitrii Solomitckii*, Vitaly Petrov*, Hosein Nikopour†, Mustafa Akdeniz†, Oner Orhan†,
Nageen Himayat†, Shilpa Talwar†, Sergey Andreev*, and Yevgeni Koucheryavy*
*Tampere University of Technology, Tampere, Finland
†Intel Labs, Santa Clara, CA, USA

***Abstract*—The use of extremely high frequency (EHF) bands, known as millimeter-wave (mmWave) frequencies, requires densification of cells to maintain system performance at required levels. This may lead to potential increase of interference in practical mmWave networks, thus making it the limiting factor. On the other hand, attractive utilization of dual-polarized antennas may improve over this situation by mitigating some of the interfering components, which can be employed as part of interference control techniques. In this paper, an accurate two-stage ray-based characterization is conducted that models interference-related metrics while taking into account a detailed dual-polarized antenna model. In particular, we confirm that narrower pencil-beam antennas (HPBW = 13°) have significant advantages as compared to antennas with relatively narrow beams (HPBW = 20° and HPBW = 50°) in the environments with high levels of interference. Additionally, we demonstrate that in the Manhattan grid deployment a transition from interference- to noise-limited regime and back occurs at the cell inter-site distances of under 90 m and over 180 m, respectively.**

## I. Introduction

A significant growth in the number of connected devices (smart phones, smart cars, etc.) and their capabilities leads to unprecedented technical challenges that need to be solved in order to provide the needed data rate, reliability, and availability. These challenges are addressed by the major stakeholders in the telecommunication sector, who currently construct the 5th generation (5G) mobile technologies. These are preparing to utilize new frequency bands above 6 GHz (termed "millimeter-wave" or "mmWave") with the bandwidth of up to 2 GHz [1].

Despite the benefits made available with larger bandwidths, mmWave frequencies have a number of specific physical properties that are different from those in existing microwave (uWave) bands employed by 3rd and 4th generation of cellular standards. Some of these properties are: significant pathloss (PL), notable penetration losses, and negligible diffraction, all effectively shrinking the coverage radius of the mmWave-based communication systems. We recall that network densification with wireless access nodes is a mainstream trend, mostly motivated by the need to increase the area spectral efficiency. Hence, small inter-site distance (ISD) between mmWave base stations (BSs) is a mandatory requirement for uninterrupted coverage. Hence, realistically, the coverage range of a single mmWave BS in urban environments will not go far beyond several hundreds of meters [2].

The use of directional antennas is another key requirement for large-scale deployment of mmWave systems. First, it allows to partly compensate for the propagation losses and significant noise levels over wider mmWave channels by keeping the coverage ranges and the ISD values at the desired levels: hundreds of meters instead of tens for omnidirectional mmWave transmissions. Second, high-gain antennas reduce the interference levels at both the user equipment (UE) and the BS sides [3], [4]. It has also been shown theoretically that mmWave systems are primarily noise-limited (in other words, the interference levels are negligible) [5].

At the same time, higher density of mmWave BSs (to further increase the area capacity) as well as the use of wider beams (due to imperfections in the beam alignment algorithms and hardware limitations) may lead to the situation, where the mmWave system begins to experience notable and significant levels of interference. Hence, the noise-limited mmWave system may transition to the interference-limited regime. Therefore, a study on appropriate scaling of interference impact in mmWave systems as a function of the BS density and antenna directivity in realistic environments is of crucial importance for the purposes of network planning and deployment optimization of costly 5G mmWave cellular networks.

There has been some literature coverage aiming to evaluate the realistic levels of interference in mmWave systems. Most of past works use either stochastic or empirical models that represent the environment as a series of random variables or equations based on pre-measured data. For instance, in [6] a stochastic performance characterization of the mmWave communication network is conducted in a constrained area with a finite number of interferers at fixed positions. Another interference-related study has been completed in [7], where a novel interference model was presented with a mixture of Inverse Gaussian and Inverse Weibull distributions.

In [5], [8], and [9] the authors investigated noise and interference limitations of the mmWave network by using empirical/stochastic approaches. In addition, [10] introduced an analytical framework for estimating the collision probability as a function of the antenna patterns and the density of simultaneously transmitting nodes. Recently, deterministic approaches to target the problem of interference modeling have been exploited by [11]. That paper presented a framework for indoor mmWave propagation modeling based on deterministic image-based ray-tracing methods to capture channel properties for specific antennas and environments having multiple transceivers.

While several works offer some insight into the behavior of interference at mmWave frequencies and the associated scaling laws, they do not take into account the specifics of mmWave equipment, such as antenna polarization issues, spatial diversity of mmWave propagation between multi-antenna arrays, as well as imperfections of the practical beamforming patterns. This in practice results in a more complex structure of the interfering signal at the receiver. While some aspects of the described problem have in part been studied by the recent works – for instance, the role of polarization diversity in MIMO systems has been investigated in [12] and the practical codebooks have been taken into account by [13], [14] – to the best of our knowledge there has been no systematic study on interference in mmWave systems, which jointly takes into account the important hardware-related aspects, including realistic antenna radiation pattern, specifics of the mmWave MIMO channel, and polarization of the antenna elements.

In this paper, we conduct this much-needed study. We first introduce our comprehensive in-house modeling framework that is capable of highly-accurate mmWave system modeling and calibrate it against reliable measurement results. We then describe the required functionality that has been developed in order to capture the transition of the mmWave system from the noise-limited to the interference-limited regime. We finally contribute and analyze the results of our performed evaluation for 28 GHz frequency band and Manhattan grid topology, by demonstrating the impact of interference for different values of ISDs and antenna radiation patterns. Our obtained numerical values are grounded in reality and can be used as a reference for calibration of both existing and future interference models for mmWave systems.

The rest of this paper is organized as follows. Our deployment scenario and the target metrics of interest are summarized in Section II. The relevant peculiarities of the mmWave propagation and the details of the utilized evaluation framework are described in Section III. Section IV is dedicated to the obtained numerical results and the corresponding discussion. The paper concludes with some general remarks offered in Section V.

## II. Target mmWave Deployment

The standard Manhattan grid scenario has been selected for our interference-centric study. This layout is representative of many real cities in the world that have modern architecture. The Manhattan grid also constitutes the basic reference topology in many wireless standardization documents, such as those by METIS [15], WINNER-II, COST, and 3GPP. However, depending on the geometrical size of buildings and the width of roads, the Manhattan grid maps may differ from each other in terms of radio signal propagation.

For consistency and to calibrate the intermediate results, we followed 3GPP with respect to the geometrical parameters of the Manhattan grid deployment [16]. Multiple mmWave BSs (169 nodes) are distributed according to the BS-grid with the equidistant step of 45 m (see Fig. 1). Since our study is focused on an outdoor case, the BSs inside buildings are not

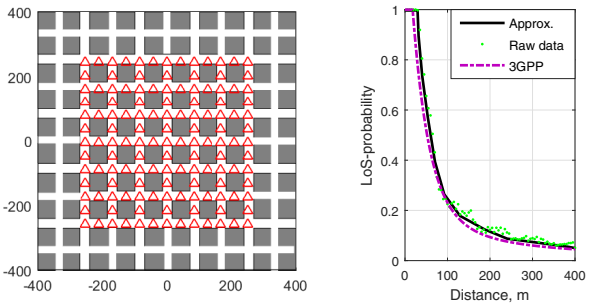


Fig. 1. Top view of the BS deployment (left) and calibration LoS-probability curves for our scenario (right). UEs are uniformly distributed across the area.

considered, which makes the total number of outdoor BSs to be 131. Similarly, we deploy the UE receivers (RXs) (their total number is 14500), where all of the indoor positions are disregarded as well. The number of outdoor RXs is hence 10500, while the distance between them is 5 m. Both the UE RX and the BS TX have 8x8 antenna arrays with double polarization, where additional details are offered in Section III. The remaining parameters are summarized in Table I.

TABLE I
Considered scenario parameters

| Parameter | Value |
|---|---|
| Total square, m | 800 x 800 |
| Propagation area, m | 600 x 600 |
| Building, m | 60 x 60 x 100 |
| Road width, m | 20 |
| Wall width, m | 0.3 |
| Wall material | concrete, $\epsilon$ = 5.03 - j0.31 [17] |
| Selected ISDs, m | 45, 90, 180, 360 |
| Selected HPBWs, ° | 13, 20, 50 |
| UE and BS heights, m | 1.5 and 10 |
| Carrier frequency, GHz | 28 |
| Bandwidth, GHz | 0.5 |
| Noise figure, dB | 7 |

Since radio interference is highly dependent on the ISD between the BSs as well as the half-power beamwidth (HPBW), different setups were considered in our simulations. To produce several distinct deployments with different densities of BSs, a dedicated function was implemented that decimates the rows and columns of the BS-grid. The mmWave carrier frequency utilized in all of our simulations is 28 GHz, which is envisioned for the initial 5G mmWave cellular deployments. The constructed scenario has also been cross-verified with the 3GPP reference data [16]. As an example, Fig. 1 (right) presents the line-of-sight (LoS) probabilities versus the distance to the BS for our deployment as compared to the reference data provided by 3GPP.

The commonly used performance metrics, such as signal-to-interference ratio (SIR) and signal-to-interference-plus-noise ratio (SINR) are considered in this work to demonstrate the effects of HPBW and density of mmWave BSs in terms of their impact on interference in urban deployments. Another question that has to be answered is that on the density of BSs and the value of HPBW, which make the mmWave system in question operate in interference- vs. noise-limited regime. The separation between these two modes is based on the parameter capturing the direct relationship between the interference and

noise powers – interference-to-noise ratio (INR). Convenient logarithmic scale helps differentiate between the two regimes as follows: $INR > 0$ dB indicates the interference-limited regime while $INR < 0$ dB corresponds to the noise-limited regime. In what follows, we focus on downlink operation.

## III. Proposed Evaluation Methodology

Generally, our methodology comprises two stages: purely deterministic ray-based modeling and post-processing on top of it to collect statistics. The first stage accurately calculates the channel properties between every TX-RX pair (TX element in the BS and RX element in the UE), while the second stage improves the results by adding a MAC abstraction and an antenna model. Such hybrid approach has a number of advantages, as compared to purely stochastic/empirical and deterministic models. First, it becomes possible to conduct a comprehensive analysis of a complex 3D deployment based on deterministic methods more efficiently. Some authors consider these tasks to be overly complex, or even impossible [18] for the purely deterministic tools. Second, in contrast to fast 2D ray-tracers [11] as well as empirical/stochastic models, our approach offers more accurate results for a specific deployment: for instance, it is feasible to accurately model the beamforming procedure when an antenna serves the selected UE.

### A. Polarization-Related Considerations

Stochastic and empirical models used by 3GPP, for instance, consider polarization as well as the metrics associated with it as a stochastic process with log-normal distribution. Such an approach may not be accurate for site-specific modeling, where polarization-related parameters can be calculated deterministically. In electromagnetic analysis, the orientation of electric (E) and magnetic (H) field vectors defines the polarization of the radio wave. Generally, polarization of the propagating wave is not strictly important with respect to the propagation of radiation in free space without any specific antenna models.

However, when an electromagnetic wave interacts with the ground or the surrounding objects, the response of the surface material can be different for various orientations of the vectors. Hence, for an accurate analysis intended in this paper, the consideration of polarization is of crucial importance. Moreover, simulation of dual-polarized antennas (two orthogonal vectors shifting by +/-$45^\circ$ to vertical orientation), which are not simply "horizontally" or "vertically" polarized, requires advanced polarization-specific considerations. Furthermore, incorrectly calculated polarization may lead to significant errors due to polarization mismatch. A general model utilized in this work represents an arbitrary oriented polarization as a sum of its horizontal and vertical components with respect to the interacting surface: $E = Ee_{||} + Ee_{\perp}$, where $e_{||}$ and $e_{\perp}$ are the orthonormal basis. This representation remains fair for reflection and diffraction physics, where ray-fixed and edge-fixed coordinate systems are used respectively (see the following subsection).

When an electromagnetic wave arrives at the RX element, the polarization loss-factor (PLF) is modeled for calibration purposes. It characterizes the cross-polarization losses between the wavefront and the RX element via an angle between these two vectors as $cos(\alpha)^2$. When the angle is $90^\circ$, then the polarization mismatch tends to infinity, while $0^\circ$ corresponds to the polarization matched case. The PLF as well as other typical wireless propagation metrics, such as cross polarization power ratio (XPR, from 3GPP specification [16]) and cross-polarized discrimination (XPD), have a similar nature and can be mapped onto each other through the components of E-field.

### B. Ray-Based Modeler

In this research, we employed our in-house ray-based modeler [19], which is a comprehensive site-specific deterministic tool for signal propagation modeling. Generally, its structure includes two parts: a physical engine calculating the radio physics and a geometrical engine establishing the propagation paths between antennas. Asymptotic high-frequency techniques based on the Geometrical Optics (GO) and the Uniform Theory of Diffraction (UTD), which are an extension of the Geometrical Theory of Diffraction (GTD), form the basis of the physical engine in our tool.

According to these theories, for wavelengths much smaller than the dimensions of the objects ($10\lambda \leq$ object size), it is possible to replace an electromagnetic wave with a line that connects the source of radiation and the receiving part [20]. Based on this premise, our geometrical engine conducts brute-force ray casting, which produces a visibility tree as well as conducts image-based ray-tracing, which calculates the paths between antennas with correct phases. Due to continuity and uniformity properties, a geodesic sphere was selected for the purposes of modeling, which produces near equidistantly positioned rays on its surfaces.

Input data for our ray-based modeler includes geometrical and physical properties of the scenario as well as the antennas. Output data from the ray-based simulation features radio channel properties in power, angular, and time domains per each TX-RX pair of elements. Our ray-based modeler supports a number of radio physics effects, which are central for the ray-based tools. The direct LoS connection between the TX-RX antenna elements separated by the distance of $r$ corresponds to the free-space propagation, which is characterized by solving the Maxwell-Helmholtz equation:

$$E(r) = E_0 \frac{e^{-j\beta r}}{r}, \tag{1}$$

where $\beta$ is the wave vector and $E_0$ is the initial E-field of antenna represented as follows:

$$E_0 = \sqrt{\frac{P_{TX} G_{TX} Z_0}{2\pi}}, \tag{2}$$

where $P_{TX}$ is the radiated power in Watts, $G_{TX}$ is the gain of the TX element, and $Z_0$ is the free-space impedance equal to $120\pi$. At the initial stage, each TX element has $G_{TX}$ = 1.

When the E-field $E^i$ falls on a surface, it reflects $E^r$ by losing some of its power. In the ray-based modeler, it is de-

scribed by a Fresnel coefficient for parallel and perpendicular orientations in relation to the plane [21]:

$$\begin{vmatrix} E_{||}^{r} \\ E_{\perp}^{r} \end{vmatrix} = \begin{vmatrix} R_{||}^{gen} & 0 \\ 0 & R_{\perp}^{gen} \end{vmatrix} \begin{vmatrix} E_{||}^{i} \\ E_{\perp}^{i} \end{vmatrix}, \tag{3}$$

where the generalized reflection coefficient for vertical and horizontal orientations relative to the plane is:

$$R_{\perp,||}^{gen} = R_{\perp,||}\,(1- \frac{(1-R_{\perp,||}^{2})\exp(-2\alpha s)\exp(-2j\beta s)\exp(jkd\sin(\theta))}{1-R_{\perp,||}^{2}\exp(-2\alpha s)\exp(-2j\beta s)\exp(jkd\sin(\theta))}\Bigg). \tag{4}$$

In (4), $\theta$ is the angle of incidence in relation to the plane's normal and $\epsilon$ is the dielectric permittivity of the material, while $\alpha$ and $\beta$ are the lossy medium propagation coefficients, $s$ is the distance traveled inside a wall, and $d$ is the gap between two adjacent rays produced by the internal reflection.

When the wavefronts interact with the smaller elements of the environment, diffuse scattering and diffraction effects occur. In this paper, we assume that diffraction takes place if a ray hits the joint of two adjacent faces located in different planes when the angle between them is not $180°$. Based on that, the diffracted field $E_d$ is described by the dyadic diffraction coefficients $D_{ss}$, $D_{sh}$, $D_{hs}$, and $D_{hh}$ as follows:

$$\begin{vmatrix} E_{\beta}^{d} \\ E_{\phi}^{d} \end{vmatrix} = \begin{vmatrix} D_{ss} & D_{sh} \\ D_{hs} & D_{hh} \end{vmatrix} \begin{vmatrix} E_{\beta}^{i} \\ E_{\phi}^{i} \end{vmatrix} \sqrt{\frac{r_{td}r_{dr}}{r_{td}+r_{dr}}} \frac{e^{-j\beta r_{dr}}}{r_{dr}}, \tag{5}$$

where $r_{td}$ is the TX to diffraction point distance, $r_{dr}$ is the diffraction point to RX distance, and $\beta$ is the wave vector [22].

The power loss of the specular component due to scattering in surface roughness is modeled by the coefficient:

$$\rho = R_{\perp,||}\exp\left(-8\pi^{2}(\sigma/\lambda)^{2}\cos(\theta)^{2}\right), \tag{6}$$

where $0 \leq \rho \leq 1$ and $\sigma$ is the roughness coefficient. To reduce simulation time, more detailed model of diffuse scattering from [23] was omitted. This simplification affects the accuracy of our output results negligibly, since power contribution from the diffuse scattering per each pair of TX-RX is small.

### C. Antenna Modeling

Broadly, an antenna model might be divided into three parts: antenna array geometry, pattern and polarization of a single element, and pre-calculated beamforming codebook. As mentioned previously, antenna geometry is based on 8x8 elements at both the BS and the UE sides with inter-element spacing of $0.5\lambda$. The central point of the array is defined as the location point. In this paper, two types of antenna arrays were investigated (see [16], Sec. 7.3): dual-polarized and single-polarized. The single-polarized antenna has 8x8 elements with the vertically oriented (along Z-axis) polarization vectors, which might be changed (e.g., to horizontal) through rotation of the utilized transformation matrix. In contrast to the single-polarized antenna, the dual-polarized antenna is modeled as two co-located elements with biased polarization vectors.

The pattern for each of the single antenna elements was adopted from the 3GPP documents (see [16], Sec. 7.3),

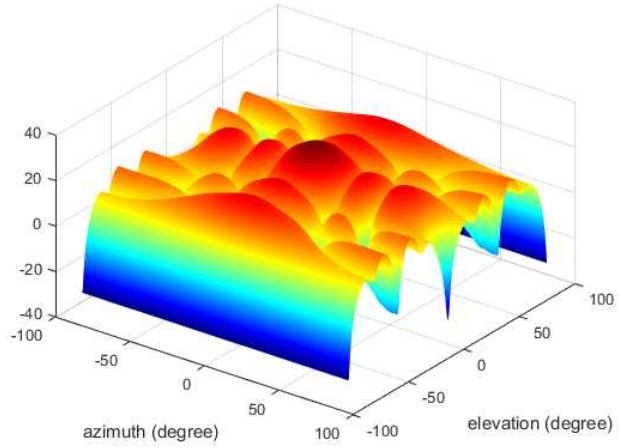


Fig. 2. Example of the pre-generated beam pattern.

while the realistic beamforming codebooks were generated beforehand (see example in Fig. 2). Three different codebooks were used in this paper for three different HPBWs: (i) HPBW = $50°$, 9 patterns; (ii) HPBW = $20°$, 81 patterns; and (iii) HPBW = $13°$, 169 patterns. The patterns were generated by taking into account mutually non-overlapping beams with a certain HPBW, which cover all of the directions in a spherical coordinate system.

Each single pattern is associated with a certain direction (azimuthal and elevation) that is represented by an array of weighted coefficients $\phi$ employed as the initial phases of the transmitted and received signal as $\exp(-\phi)$. Based on the angular properties of dominant paths, appropriate patterns were selected and assigned to both the BS and the UE sides.

### D. MIMO Channel Model

MIMO channel relies on the availability of multiple decorrelated RF-channels on the side of both the UE and the BS for the purposes of improving the channel diversity. In this work, we consider two antennas: single-polarized for calibration purposes and dual-polarized for main simulations. In case of two single-polarized 8x8 element antennas on the BS and the UE sides, 64x64 channels were produced:

$$\begin{bmatrix} x_1 \\ x_2 \\ x_3 \\ \vdots \\ x_{64} \end{bmatrix} = \begin{bmatrix} h_{1,1} & h_{1,2} & \cdots & h_{1,64} \\ h_{2,1} & h_{2,2} & \cdots & h_{2,64} \\ h_{3,1} & h_{3,2} & \cdots & h_{3,64} \\ \vdots & \vdots & \vdots & \ddots & \vdots \\ h_{64,1} & h_{64,2} & \cdots & h_{64,64} \end{bmatrix} \times \begin{bmatrix} y_1 \\ y_2 \\ y_3 \\ \vdots \\ y_{64} \end{bmatrix}. \tag{7}$$

Since one dual-polarized antenna is represented as a combination of two collocated 8x8 arrays with mutually orthogonal vectors of polarization, the number of channels between a single UE and the BS increases as well:

$$\begin{bmatrix} x_1 \\ x_2 \\ x_3 \\ \vdots \\ x_{128} \end{bmatrix} = \begin{bmatrix} h_{1,1} & h_{1,2} & \cdots & h_{1,128} \\ h_{2,1} & h_{2,2} & \cdots & h_{2,128} \\ h_{3,1} & h_{3,2} & \cdots & h_{3,128} \\ \vdots & \vdots & \ddots & \vdots \\ h_{64,1} & h_{64,2} & \cdots & h_{128,128} \end{bmatrix} \times \begin{bmatrix} y_1 \\ y_2 \\ y_3 \\ \vdots \\ y_{128} \end{bmatrix}. \tag{8}$$

By default, our ray-based modeler can simulate MISO channels straightforwardly, which may take significant time when utilizing multiple antennas. As the number of TX antenna elements increases by $N$-times, the tool needs to calculate the channel just as often.

To mitigate this complexity, we simplify the modeling such that it would not require channel recalculation for each element of the antenna. Considering that most of the modeling time is spent on the geometrical considerations to find the path between each pair of TX and RX, we make the following assumption. Due to the fact that the size of the antenna array is much smaller than that of the script objects, the paths of all elements interact with the same elements of the scenario. In other words, by constructing the visibility tree for one transmit element, we can map it onto other elements within the same antenna as well. At the same time, the way points are kept unique for each TX-RX pair.

### E. MAC Layer Abstraction

As soon as all the necessary channel information is collected between each isotropic TX-RX pair, the following stage begins. The main goal here is to calculate the interference metrics, such as the SIR and INR values, by using the detailed antenna models and MAC-abstraction represented e.g., by a Round-Robin scheduling algorithm. Prior to these operations, the beamforming codebooks are pre-calculated and stored for HPBW = 13°, 20°, and 50°. The weight phase coefficients are utilized further on to achieve the beam alignment between the BS and the UE. The post-processing phase starts by sorting: the BS having the dominant path (i.e., the highest power) to the UE with respect to other BSs is assumed to be the serving one. Using the path sorting procedure, for each of the BSs a group of the relevant UEs is assigned. Fig. 3 demonstrates the links as a "star" topology between the BSs and their served UEs. In most cases, the distance is the measure that determines which of the BSs the user belongs to. On the other hand, there are cases when – due to certain physical phenomena (e.g., interference) – the UE can be served by a more remote BS.

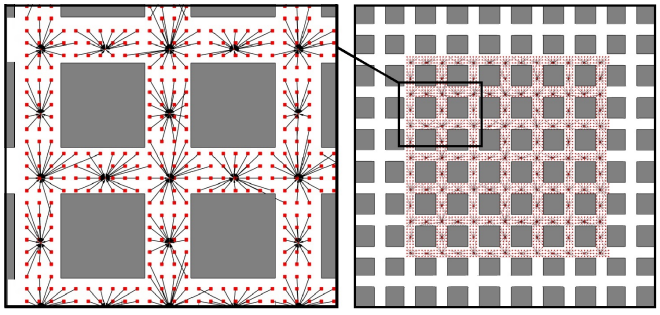

Fig. 3. UEs (red dots) collected in a group, each of which is served by a single BS. Such BS-UE links are represented as a "star" topology.

Finally, Round-Robin considerations are applied, which play the role of a MAC-abstraction in our simulations. From the stored list of UEs, each BS selects one and directs its main beam according to the departure angles (elevation and azimuth) from which the maximum receive power arrives.

## IV. Representative Numerical Results

### A. LoS Calibration of Polarization Model

Before conducting our interference study, it is important to calibrate the antenna model, which is based on the classical Maxwell EM equations. A simple deployment was selected, where TX and RX antennas are aligned to each other in the LoS-conditions without any additional obstacles around them. Such alignment follows the equation (1). To verify the polarization modeling, the RX array was rotated with the step of 20° in relation to the TX antenna in the angular range of -90...90° (see Fig.4). In case of one TX and one RX dipoles, cross-polarization occurs when the relative angle is 90°, which corresponds to the theoretical model.

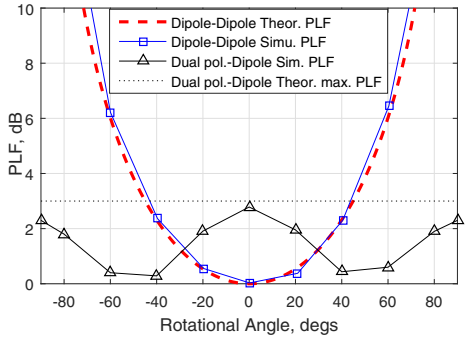


Fig. 4. Rotation of dual-polarized and single-polarized antennas relative to each other produces different magnitudes of polarization loss.

In case of utilizing dual-polarized antenna, two LoS-channels emerge: $TX{-}RX_{-45}$ and $TX{-}RX_{+45}$. Such complementary channels make the maximum PLF to be $\leq 3$ dB, which also agrees with the theoretical value. Here, summation of the two received signals after RF processing makes the polarization loss to be negligible. When dual-polarized antennas are located on the TX and RX sides, four different channels can be observed. The availability of second TX channel increases the total received power on a single RX element by extra 3 dB.

### B. Polarization Model Calibration in Manhattan Grid

As soon as LoS calibration between the antennas is completed, calibration in the Manhattan grid deployment becomes the next step. For this purpose, single-polarized (horizontal and vertical) antennas as well as dual-polarized antennas were utilized in our simulations. Output data from these simulations are represented by three different PLs: horizontally polarized PL (h-pol. PL), vertically polarized PL (v-pol. PL), and dual polarized PL (x-pol. PL). These three PLs should be considered separately, since the corresponding Fresnel coefficients (and their combination) are different.

To validate our preliminary expectations, Fig. 5 demonstrates log-approximated PL data. The difference between the h-pol. PL and the v-pol. PL is up to 12 dB, which is primarily caused by reflection losses. At the same time, being a combination of both v-pol and h-pol, x-pol PL is located in-between. Due to low polarization losses and possibility

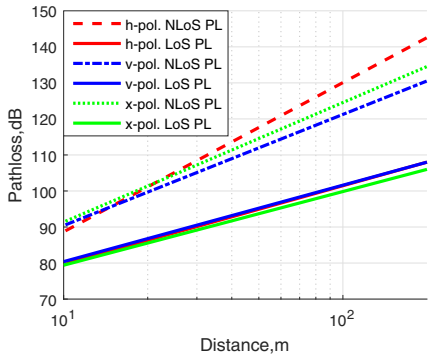


Fig. 5. Behavior of pathloss is different for vertical and horizontal polarization as well as for dual-polarized antenna.

to implement the polarization diversity for mmWave MIMO system, x-pol antenna has been selected and used in our further numerical evaluations.

### C. Interference Analysis

After the antenna model has been verified, further investigation of interference is conducted at different densities of BSs and for variable beamwidths. Particularly, we focus on the CDFs of SIR values in Fig. 6 and the mean values of SINR in Fig. 7. First, when the HPBW is 13°, the highest SIR and SINR values are observed with respect to the HPBW of 20° and 50°. Hence, narrower beams improve both SIR and SINR, since a lower fraction of interfering signals comes to the main beam of the target RX.

Second, there are two competing trends as the ISD begins to increase: the useful signal from the target BS becomes weaker (since the average distance to the BS grows), but also the density of interfering BSs decreases, thus the total power of the interfering components degrades. It has been shown in [4] that the first trend is stronger in free space, so the SIR and SINR values should degrade with the increase of ISD. Here, we can confirm this observation for a practical mmWave deployment in the Manhattan grid topology.

However, the decrease in question is not linear, since the difference between the SINR for HPBW = 13°, 45 m ISD and the SINR for HPBW = 13°, 360 m ISD is over 14 dB, while the same difference for HPBW = 20° is around 2 dB and less than 1 dB for HPBW = 50°. In other words, depending on the target HPBW value, the response of the mmWave system to densification is different, which suggests exploring the difference between the interference-limited and the noise-limited regimes.

### D. Noise- vs. Interference-Limited Regimes

As mentioned above, there are two extreme regimes that the mmWave system may operate in: interference-limited and noise-limited. While the majority of past studies agree that an idealistic mmWave deployment (propagation in open space, narrow beams, perfect beam alignment, etc.) may operate in close to noise-limited regime, we have observed that the impact of interference may remain significant in certain cases.

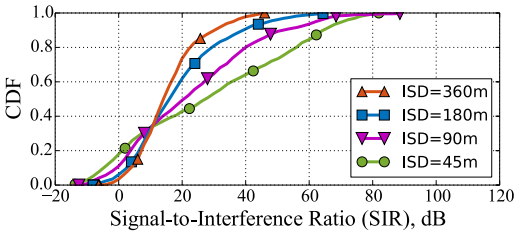


(a) HPBW = 50°

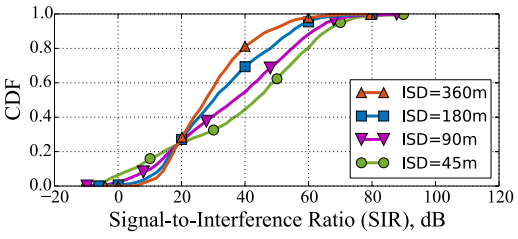


(b) HPBW = 20°

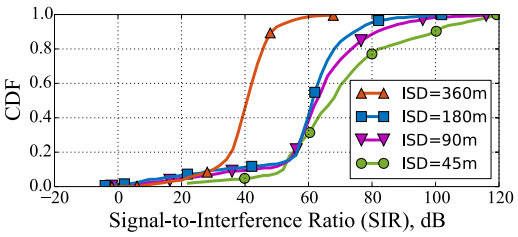


(c) HPBW = 13°

Fig. 6. CDF of SIR for various densities of BSs and HPBWs.

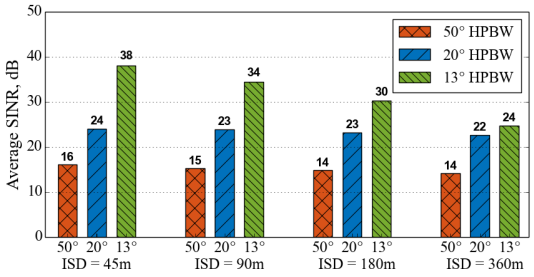


Fig. 7. Mean values of SINR for various densities of BSs and HPBWs.

We continue our numerical study by analyzing the scaling of the representative INR metric, which directly corresponds to the ratio between the levels of interference and noise in the considered system. Particularly, Fig. 8 demonstrates the complementary cumulative distribution function (CCDF) for the INR values in various deployment cases. Observing Fig. 8, we first notice that there are three deployments for which more than 80% of the RXs are in the noise-limited regime ($INR <$ 0 dB): all with HPBW= 13°, but at different ISDs. At the same time, there are other three curves for which more than 80% of the RXs are in the interference-limited regime ($INR >$ 0 dB), two of which with HPBW= 50° and ISDs equal to 45 m. Other deployments are in the intermediate regime, where neither noise nor interference dominate across all of the UEs.

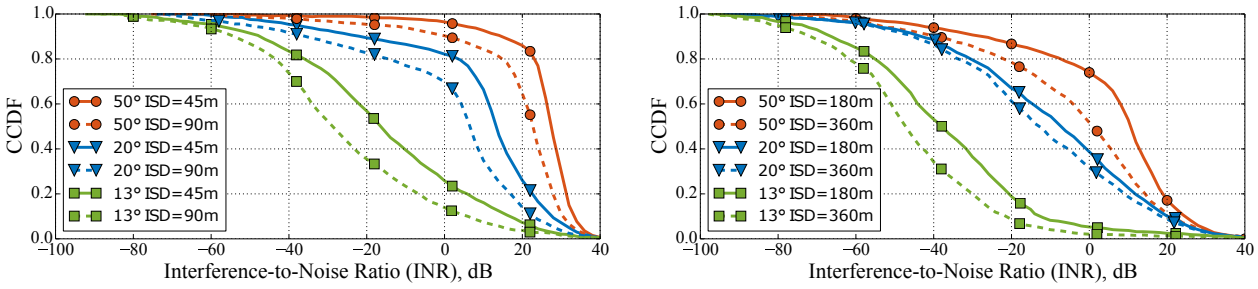


(a) 45 m and 90 m ISD

(b) 180 m and 360 m ISD

Fig. 8. CCDF of INR for four densities of BSs and three HPBWs.

## V. Conclusions

In this paper, we studied the role of interference in the mmWave systems as a function of the deployment parameters, such as the inter-site distance between the base stations and the beamwidth of the antenna radiation pattern. For this matter, we developed a comprehensive ray-based modeling methodology that takes into account not only the geometrical and physical properties of the scenario, but also the specifics of the received mmWave signal impacted by realistic antenna polarization, practical antenna radiation patterns, as well as MIMO mmWave channel.

With our developed tool, we evaluated the impact of interference in various deployment configurations of the 28 GHz mmWave cellular system in the Manhattan grid topology, by obtaining the averages and the CDFs of SIR and INR values. We also illustrated how the clearly noise-limited operation with 360 m ISD and 13° beamwidth transitions into a distinct interference-limited regime with 45 m ISD and 50° beamwidth. These results may become a reference for future deployment optimization of mmWave cellular networks as well as for verification/calibration of more flexible (but typically less accurate, e.g., stochastic) mmWave interference models. At the same time, our systematically described evaluation methodology may be applied for site-specific studies of complex and practical mmWave scenarios.

## Acknowledgement

This work is supported by Intel Corporation as well as by the project TT5G: Transmission Technologies for 5G.

## References

[1] S. Rangan, T. S. Rappaport, and E. Erkip, "Millimeter-wave cellular wireless networks: Potentials and challenges," *Proceedings of the IEEE*, vol. 102, pp. 366–385, March 2014.

[2] M. N. Kulkarni, S. Singh, and J. G. Andrews, "Coverage and rate trends in dense urban mmWave cellular networks," in *Proc. of IEEE GLOBECOM*, December 2014.

[3] K. Venugopal, M. C. Valenti, and R. W. Heath, "Device-to-Device millimeter wave communications: Interference, coverage, rate, and finite topologies," *IEEE Transactions on Wireless Communications*, vol. 15, pp. 6175–6188, September 2016.

[4] V. Petrov, M. Komarov, D. Moltchanov, J. M. Jornet, and Y. Koucheryavy, "Interference and SINR in millimeter wave and terahertz communication systems with blocking and directional antennas," *IEEE Transactions on Wireless Communications*, vol. 16, pp. 1791–1808, March 2017.

[5] J. G. Andrews, T. Bai, M. N. Kulkarni, A. Alkhateeb, A. K. Gupta, and R. W. Heath, "Modeling and analyzing millimeter wave cellular systems," *IEEE Transactions on Communications*, vol. 65, pp. 403–430, January 2017.

[6] K. Venugopal, M. C. Valenti, and R. W. Heath, "Interference in finite-sized highly dense millimeter wave networks," in *Proc. of Information Theory and Applications Workshop (ITA)*, pp. 175–180, February 2015.

[7] H. Elkotby and M. Vu, "A mixture model for NLOS mmWave interference distribution," in *Proc. of IEEE GLOBECOM*, December 2016.

[8] H. Shokri-Ghadikolaei and C. Fischione, "Millimeter wave ad hoc networks: Noise-limited or interference-limited?," in *Proc. of IEEE Globecom Workshops*, December 2015.

[9] M. Rebato, M. Mezzavilla, S. Rangan, F. Boccardi, and M. Zorzi, "Understanding noise and interference regimes in 5G millimeter-wave cellular networks," in *Proc. of European Wireless Conference*, May 2016.

[10] S. Singh, R. Mudumbai, and U. Madhow, "Interference analysis for highly directional 60-GHz mesh networks: The case for rethinking medium access control," *IEEE/ACM Transactions on Networking*, vol. 19, pp. 1513–1527, October 2011.

[11] D. Steinmetzer, J. Classen, and M. Hollick, "mmTrace: Modeling millimeter-wave indoor propagation with image-based ray-tracing," in *Proc. of IEEE INFOCOM Workshops*, pp. 429–434, April 2016.

[12] J. Song, J. Choi, S. G. Larew, D. J. Love, T. A. Thomas, and A. A. Ghosh, "Adaptive millimeter wave beam alignment for dual-polarized MIMO systems," *IEEE Transactions on Wireless Communications*, vol. 14, pp. 6283–6296, November 2015.

[13] U. Schmid, D. Lin, and W. Menzel, "A novel dual polarization antenna array fed by a dual mode non-radiative dielectric waveguide," in *IEEE/MTT-S International Microwave Symposium Digest*, pp. 1–3, June 2012.

[14] J. Wu, S. Yang, Y. Chen, S. Qu, and Z. Nie, "A low profile dual-polarized wideband omnidirectional antenna based on AMC reflector," *IEEE Transactions on Antennas and Propagation*, vol. 65, pp. 368–374, January 2017.

[15] "METIS channel models," Tech. Rep. ICT-317669-METIS/D1.4, METIS, February 2015.

[16] 3GPP, "Channel model for frequency spectrum above 6 GHz (Release 14)," 3GPP TR 38.900 V2.0.0, 2016.

[17] "Effects of building materials and structures on radiowave propagation above about 100 MHz," *ITU-R P.2040-1*, July 2015.

[18] F. Baccelli and B. Blaszczyszyn, *Electromagnetics of Body Area Networks: Antennas, Propagation, and RF Systems*. Wiley, 2016.

[19] V. Petrov, D. Solomitckii, A. Samuylov, M. A. Lema, M. Gapeyenko, D. Moltchanov, S. Andreev, V. Naumov, K. Samouylov, M. Dohler, and Y. Koucheryavy, "Dynamic multi-connectivity performance in ultra-dense urban mmwave deployments," *IEEE Journal on Selected Areas in Communications*, vol. 35, pp. 2038–2055, September 2017.

[20] H. Singh and R. M. Jha, *Active Radar Cross Section Reduction*. Cambridge University Press, 2015.

[21] L. M. Correia and P. O. Frances, "Estimation of materials characteristics from power measurements at 60 GHz," in *Proc. of IEEE PIMRC*, September 1994.

[22] P. D. Holm, "A new heuristic UTD diffraction coefficient for non-perfectly conducting wedges," *IEEE Transactions on Antennas and Propagation*, vol. 48, pp. 1211–1219, August 2000.

[23] V. Degli-Esposti, D. Guiducci, A. de'Marsi, P. Azzi, and F. Fuschini, "An advanced field prediction model including diffuse scattering," *IEEE Transactions on Antennas and Propagation*, vol. 52, pp. 1717–1728, July 2004.